




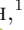




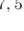
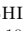
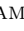














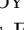
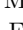

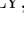

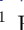
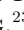

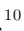

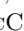





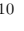

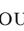



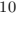
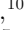

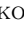
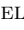


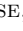




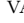








## Direct Optimal Mapping Image Power Spectrum and its Window Functions

ZHILEI XU <sup>1</sup>, HONGGEUN KIM <sup>1,2</sup>, JACQUELINE N. HEWITT <sup>1,2</sup>, KAI-FENG CHEN <sup>1,2</sup>, NICHOLAS S. KERN <sup>1,2,3</sup>,  
ELIZABETH RATH <sup>1,2</sup>, RUBY BYRNE <sup>4</sup>, ADÉLIE GORCE <sup>5</sup>, ZACHARY E. MARTINOT <sup>6</sup>, JOSHUA S. DILLON <sup>7</sup>,  
BRYNA J. HAZELTON <sup>8,9</sup>, ADRIAN LIU <sup>7,5</sup>, MIGUEL F. MORALES <sup>8</sup>, ZARA ABDURASHIDOVA <sup>7</sup>, TYRONE ADAMS <sup>10</sup>,  
JAMES E. AGUIRRE <sup>6</sup>, PAUL ALEXANDER <sup>11</sup>, ZAKI S. ALI <sup>7</sup>, RUSHELLE BAARTMAN <sup>10</sup>, YANGA BALFOUR <sup>10</sup>,  
ADAM P. BEARDSLEY <sup>12,13</sup>, GIANNI BERNARDI <sup>14,15,10</sup>, TASHALEE S. BILLINGS <sup>6</sup>, JUDD D. BOWMAN <sup>12</sup>,  
RICHARD F. BRADLEY <sup>16</sup>, PHILIP BULL <sup>17,18</sup>, JACOB BURBA <sup>17</sup>, STEVEN CAREY <sup>11</sup>, CHRIS L. CARILLI <sup>19</sup>,  
CARINA CHENG <sup>7</sup>, DAVID R. DEBOER <sup>20</sup>, ELOY DE LERA ACEDO <sup>11</sup>, MATT DEXTER <sup>20</sup>, NICO EKSTEEN <sup>10</sup>, JOHN ELY <sup>11</sup>,  
AARON EWALL-WICE <sup>7,21</sup>, NICOLAS FAGNONI <sup>10</sup>, RANDALL FRITZ <sup>10</sup>, STEVEN R. FURLANETTO <sup>22</sup>,  
KINGSLEY GALE-SIDES <sup>11</sup>, BRIAN GLENDENNING <sup>23</sup>, DEEPTHI GORTHI <sup>7</sup>, BRADLEY GREIG <sup>24</sup>, JASPER GROBBELAAR <sup>10</sup>,  
ZIYAAD HALDAY <sup>10</sup>, JACK HICKISH <sup>20</sup>, DANIEL C. JACOBS <sup>12</sup>, AUSTIN JULIUS <sup>10</sup>, MACCALVIN KARISEB <sup>10</sup>,  
JOSHUA KERRIGAN <sup>25</sup>, PIYANAT KITTIWISIT <sup>18</sup>, SAUL A. KOHN <sup>6</sup>, MATTHEW KOLOPANIS <sup>12</sup>, ADAM LANMAN <sup>25</sup>,  
PAUL LA PLANTE <sup>7,6</sup>, ANITA LOOTS <sup>10</sup>, DAVID HAROLD EDWARD MACMAHON <sup>20</sup>, LOURENCE MALAN <sup>10</sup>,  
CRESSHIM MALGAS <sup>10</sup>, KEITH MALGAS <sup>10</sup>, BRADLEY MARERO <sup>10</sup>, ANDREI MESINGER <sup>26</sup>, MATHAKANE MOLEWA <sup>10</sup>,  
TSHEGOFALANG MOSIANE <sup>10</sup>, STEVEN G. MURRAY <sup>12</sup>, ABRAHAM R. NEBEN <sup>1,2</sup>, BOJAN NIKOLIC <sup>11</sup>, HANS NUWEGELD <sup>10</sup>,  
AARON R. PARSONS <sup>7</sup>, NIPANJANA PATRA <sup>7</sup>, SAMANTHA PIETERSE <sup>10</sup>, NIMA RAZAVI-GHODS <sup>11</sup>, JAMES ROBNETT <sup>19</sup>,  
KATHRYN ROSIE <sup>10</sup>, PETER SIMS <sup>5</sup>, CRAIG SMITH <sup>10</sup>, HILTON SWARTS <sup>10</sup>, NITHYANANDAN THYAGARAJAN <sup>27</sup>,  
PIETER VAN WYNGAARDEN <sup>10</sup>, PETER K. G. WILLIAMS <sup>28,29</sup> AND HAOXUAN ZHENG<sup>2</sup>

(HERA COLLABORATION)

<sup>1</sup>MIT Kavli Institute, Massachusetts Institute of Technology, Cambridge, MA

<sup>2</sup>Department of Physics, Massachusetts Institute of Technology, Cambridge, MA

<sup>3</sup>NHFP Hubble Fellow

<sup>4</sup>Cahill Center for Astronomy and Astrophysics, California Institute of Technology, Pasadena, CA

<sup>5</sup>Department of Physics and McGill Space Institute, McGill University, 3600 University Street, Montreal, QC H3A 2T8, Canada

<sup>6</sup>Department of Physics and Astronomy, University of Pennsylvania, Philadelphia, PA

<sup>7</sup>Department of Astronomy, University of California, Berkeley, CA

<sup>8</sup>Department of Physics, University of Washington, Seattle, WA

<sup>9</sup>eScience Institute, University of Washington, Seattle, WA

<sup>10</sup>South African Radio Astronomy Observatory, Black River Park, 2 Fir Street, Observatory, Cape Town, 7925, South Africa

<sup>11</sup>Cavendish Astrophysics, University of Cambridge, Cambridge, UK

<sup>12</sup>School of Earth and Space Exploration, Arizona State University, Tempe, AZ

<sup>13</sup>Department of Physics, Winona State University, Winona, MN

<sup>14</sup>INAF-Istituto di Radioastronomia, via Gobetti 101, 40129 Bologna, Italy

<sup>15</sup>Department of Physics and Electronics, Rhodes University, PO Box 94, Grahamstown, 6140, South Africa

<sup>16</sup>National Radio Astronomy Observatory, Charlottesville, VA

<sup>17</sup>Jodrell Bank Centre for Astrophysics, University of Manchester, Manchester, M13 9PL, United Kingdom

<sup>18</sup>Department of Physics and Astronomy, University of Western Cape, Cape Town, 7535, South Africa

<sup>19</sup>National Radio Astronomy Observatory, Socorro, NM 87801, USA

<sup>20</sup>Radio Astronomy Lab, University of California, Berkeley, CA

<sup>21</sup>Department of Physics, University of California, Berkeley, CA

<sup>22</sup>Department of Physics and Astronomy, University of California, Los Angeles, CA

<sup>23</sup>National Radio Astronomy Observatory, Socorro, NM

<sup>24</sup>School of Physics, University of Melbourne, Parkville, VIC 3010, Australia

<sup>25</sup>Department of Physics, Brown University, Providence, RI

<sup>26</sup>Scuola Normale Superiore, 56126 Pisa, PI, Italy

Corresponding author: Zhilei Xu (徐智磊)

zhileixu@mit.edu

zhileixu@space.mit.edu

<sup>27</sup> Commonwealth Scientific and Industrial Research Organisation (CSIRO), Space & Astronomy, P. O. Box 1130, Bentley, WA 6102, Australia

<sup>28</sup> Center for Astrophysics, Harvard & Smithsonian, Cambridge, MA

<sup>29</sup> American Astronomical Society, Washington, DC

## ABSTRACT

The key to detecting neutral hydrogen during the epoch of reionization (EoR) is to separate the cosmological signal from the dominating foreground radiation. We developed direct optimal mapping (Xu et al. 2022) to map interferometric visibilities; it contains only linear operations, with full knowledge of point spread functions from visibilities to images. Here we present an FFT-based image power spectrum and its window functions based on direct optimal mapping. We use noiseless simulation, based on the Hydrogen Epoch of Reionization Array (HERA) Phase I configuration, to study the image power spectrum properties. The window functions show  $< 10^{-11}$  power leakage from the foreground-dominated region into the EoR window; the 2D and 1D power spectra also verify the separation between the foregrounds and the EoR. Furthermore, we simulated visibilities from a  $uv$ -complete array and calculated its image power spectrum. The result shows that the foreground–EoR leakage is further suppressed below  $10^{-12}$ , dominated by the tapering function sidelobes; the 2D power spectrum does not show signs of the horizon wedge. The  $uv$ -complete result provides a reference case for future 21 cm cosmology array designs.

*Keywords:* 21-cm lines (690), Early universe (435), Radio interferometry (1346), Reionization (1383)

## 1. INTRODUCTION

Recent cosmological observations have established the standard cosmological model —  $\Lambda$ CDM cosmology (Bennett et al. 1996; Riess et al. 1998; Bennett et al. 2013; Hinshaw et al. 2013; Planck Collaboration et al. 2016, 2020). The cosmic microwave background (CMB) measures the early universe at redshift  $\sim 1100$  (Fixsen et al. 1996; Hu & Dodelson 2002; Staggs et al. 2018); the late universe measurement gives statistical properties of the universe below redshift 10 (Anderson et al. 2014; Alam et al. 2017; Abbott et al. 2022; More et al. 2023). However, we have hardly observed the universe from redshift 1100 to 10, including dark ages, cosmic dawn, and the epoch of reionization (EoR) (Furlanetto et al. 2006; Pritchard & Loeb 2012).

With measurements from the initial ( $z \sim 1100$ ) and final ( $z < 10$ ) conditions, the  $\Lambda$ CDM cosmology describes the initial perturbations’ growth from linear to non-linear until the ignition of first stars and galaxies (Hogan & Rees 1979; Madau et al. 1997). Our goal is to observe this process by measuring radiation from the dominant baryonic content in the universe — neutral hydrogen. The atomic hyperfine structure of neutral hydrogen leads to emission or absorption of 21 cm radiation in the restframe. The 21 cm radiation, redshifted, is observed at different frequency channels, tracing the distribution of the baryonic matter during EoR, cosmic dawn, and dark ages. Direct observations covering the above epochs are the ultimate goal of 21 cm cosmology.

The 21 cm observations have the potential to measure a wide range of cosmological history, testing the current cosmological model (Mao et al. 2008). The result will reveal more details of the cosmological evolution and the universe’s contents, including dark matter and dark energy.

In practice, wavelengths of high-redshift 21 cm radiation are redshifted to  $> 2$  m beyond  $z \sim 8.5$ ; correspondingly,  $> 230$  m baselines are required to achieve  $\sim 0.5^\circ$  angular resolutions. Therefore, high-redshift 21 cm measurements are conducted with interferometers for angular resolutions (Parsons et al. 2010; Tingay et al. 2013; van Haarlem et al. 2013; DeBoer et al. 2017). Interferometers are also cost-effective in achieving large collecting areas, which eventually determines the measurement sensitivity. Using interferometers, we aim to measure the distribution of neutral hydrogen radiation across the sky with power spectra. Image-based power spectra are measured in both CMB (Bennett et al. 2013; Planck Collaboration et al. 2020) and other 21 cm experiments (Dillon et al. 2014, 2015; Beardsley et al. 2016; Trott et al. 2016; Patil et al. 2017; Barry et al. 2019; Li et al. 2019; Rahimi et al. 2021). Here we present one power spectrum estimator based on direct optimal mapping (Xu et al. 2022, hereafter X22).

In this paper, we study the image power spectrum based on one interferometer array — the Hydrogen Epoch of Reionization Array (HERA) (Pober et al. 2014; DeBoer et al. 2017) — and calculate the image power

spectrum and its window functions. The frequency coverage provides a tomographic measurement of the Epoch of Reionization (EoR), constraining the evolution of neutral hydrogen spin temperature and ionization fraction during EoR (Furlanetto et al. 2006; Morales & Wyithe 2010; Pritchard & Loeb 2012; Liu & Shaw 2020). These measurements also constrain sources for the reionization process, including UV and X-ray properties of high-redshift galaxies (Ewall-Wice et al. 2016; Greig et al. 2016; Kern et al. 2017).

Section 2 introduces the image power spectrum concept and presents the mathematical formalism of the image power spectrum and its window functions. In Section 3, we first introduce the image cube, constructed with direct optimal mapping, and present the results for the window functions, 2D power spectrum, and 1D power spectrum. In Section 4, we further explore the potential of this image power spectrum by simulating visibilities from a  $uv$ -complete array and investigating its image power spectrum. We discuss future work in Section 5 before concluding in Section 6. We use the *WMAP* nine-year cosmology (Bennett et al. 2013) throughout this paper.

## 2. IMAGE POWER SPECTRUM

The key challenge for 21 cm cosmology is to detect the EoR signals with the presence of foregrounds, which have intensity at least four orders of magnitude brighter than the cosmological signals (Liu et al. 2014). Fortunately, the foreground and the EoR signals have different frequency properties with *pixels*: foregrounds have smooth frequency spectra while the EoR signals have both smooth and fast-changing components. One essential question is how well different analyses can separate EoR from smooth foregrounds, and detect EoR in the region of Fourier space expected to be free of foreground emission, called the *EoR window*.

The raw data from an interferometer are the cross-correlations among antenna pairs, called visibilities. Visibilities are measured at different frequency channels, among which the instrument intrinsically has different spatial responses, called instrumental chromaticity. This instrumental chromaticity converts spatial structures into the frequency axis, causing the visibility frequency spectrum to contain not only the pixel frequency spectrum but also the features leaked in from spatial structures. If we calculate the frequency Fourier Transform of the visibilities, we see not only the frequency spectrum of sky pixels but also their spatial structures, mostly from the foregrounds. The latter component contributes to the ‘wedge’ feature in the 2D power spectrum (Datta et al. 2010; Parsons et al. 2012;

Parsons et al. 2012; Liu et al. 2014; Liu et al. 2014). The technique of measuring the power spectrum by Fourier Transforming the visibility’s frequency axis is called the delay power spectrum. (Parsons et al. 2012).

Alternatively, part of the instrumental chromaticity can be accounted for by analyzing frequency spectra of *pixels*, instead of visibilities. Therefore, this approach is called image power spectrum (Morales & Hewitt 2004; Liu & Tegmark 2011; Dillon et al. 2013). Analyzing sky pixels mitigates the space-to-frequency leakage from the visibilities. Morales et al. (2019) investigated the two approaches and concluded that, assuming uniform  $uv$  coverage, the image power spectrum achieves lower foreground leakage into the wedge than the delay power spectrum.

However, working with pixels requires forming a 3D image cube from the visibilities. Fundamentally, the imaging process presents the visibilities in a linear combination that minimize the instrumental chromaticity. How much instrumental chromaticity can be accounted for with imaging depends on how much information we possess to reconstruct the sky. If we had perfect knowledge of the primary beam, its effect could be eliminated in imaging, removing the primary beam chromaticity; if we had complete  $uv$ -coverage, we could reconstruct each sky pixel without degeneracy, removing chromaticity from interferometric grating lobes.

Our image power spectrum is based on direct optimal mapping (X22). In contrast to other imaging algorithms (Högbom 1974; Clark 1980; Cornwell 2008; Rau & Cornwell 2011), our mapping method does not include iterative processes. In addition, we map the visibility data at their original  $uv$  locations without gridding (Sullivan et al. 2012). The algorithm involves only linear operations, robustly tracking the transfer function in the process; both the point spread function and the pixel covariance matrix can be accurately calculated during the mapping process. We then calculate the power spectra from the image cube, and the point spread function is used to calculate the power spectrum window functions.

In practice, interferometers rarely achieve complete and uniform  $uv$  coverage, meaning that the observations do not contain sufficient information to recover pixel intensities without ambiguity. This ambiguity shows up as grating lobes in images, which keeps us from achieving the ideal spectral leakage mitigation. Now the questions are how much mitigation one can achieve by image power spectrum with a realistic interferometer, and how much more one can achieve with a  $uv$ -complete interferometer. This paper addresses the two questions in the following sections.

### 2.1. Power Spectrum Definition

We first present the power spectrum formula and discuss the symmetry assumptions for constructing a power spectrum and binning a 3D power spectrum into 2D and 1D.

With a 3D image cube, we calculate its 3D discrete Fourier Transform (DFT) following the convention in Mesinger & Furlanetto (2007):

$$\tilde{m}(\mathbf{k}) = \frac{V}{N} \sum m(\mathbf{r}) e^{-i\mathbf{k}\cdot\mathbf{r}}, \quad (1)$$

where  $m(\mathbf{r})$  contains the intensity of the image cube and  $\mathbf{r}$  is the 3D spatial vector,  $\tilde{m}(\mathbf{k})$  is the DFT of the image cube and  $\mathbf{k}$  is the 3D wavenumber vector,  $V$  is the physical size of the image cube (in the unit of  $\text{Mpc}^3 \cdot \text{h}^{-3}$ ), and  $N$  is the number of voxels.

The power spectrum is calculated by squaring the DFT result and dividing out the total volume of the image cube (Liu & Shaw 2020)

$$P(\mathbf{k}) = \frac{\langle \tilde{m}(\mathbf{k})^* \cdot \tilde{m}(\mathbf{k}) \rangle}{V}. \quad (2)$$

For spatially homogeneous signals, like cosmological signals from the early universe, all cross terms from  $\langle \tilde{m}(\mathbf{k}')^* \cdot \tilde{m}(\mathbf{k}) \rangle$ , when  $\mathbf{k}' \neq \mathbf{k}$ , average to zero. Our observable universe is one realization from its underlying power spectrum. The angle brackets indicate that the true power spectrum is defined as the average over sufficient realizations of the universe. The angle brackets only apply to the variables with randomness. For a deterministic variable, the angled value equals itself, say the image cube volume  $\langle V \rangle = V$ .

The power spectrum is originally expressed in 3D  $\mathbf{k}$  space. We bin the 3D power spectrum to 2D (or 1D) under different symmetry assumptions. For the 2D binning, the two dimensions perpendicular to the line-of-sight (LOS) are circularly binned into  $k_\perp$ , assuming the two perpendicular dimensions share the same statistical properties. Together with  $k_\parallel$ , parallel to LOS, we form the 2D  $k_\perp - k_\parallel$  power spectrum, which is the natural space for foreground avoidance (Datta et al. 2010; Morales et al. 2012; Parsons et al. 2012). For the 1D binning, we assume isotropy of the signal, and all three dimensions are spherically binned into one dimension; the 3D vector  $\mathbf{k}$  is condensed to only its length  $k$ . Since the cosmological signals are believed to be homogeneous and isotropic at large scales, the 1D binning is often used to describe the power spectrum of the cosmological signals.

Homogeneity and isotropy in cosmological signals ensure the validity of the above steps; however, when the foregrounds are involved, which can be neither homoge-

neous nor isotropic, one should be aware of the underlying assumptions as we reduce power spectrum dimensions.

### 2.2. Power Spectrum Estimator

We form an estimated image cube with the direct optimal mapping algorithm. Here we quickly review the method and refer to more details presented in X22. We first create the data model of the visibilities as

$$\mathbf{d}_{f_i} = \mathbf{A}_{f_i} \mathbf{m}_{f_i} + \mathbf{n}_{f_i}, \quad (3)$$

where  $\mathbf{d}_{f_i}$  is the measured data at the frequency channel  $f_i$ ,  $\mathbf{m}_{f_i}$  is the true sky emission at the frequency channel,  $\mathbf{A}_{f_i}$  is the measurement matrix which describes how the interferometer integrates sky emission to produce visibilities, and  $\mathbf{n}_{f_i}$  represents noise in the visibilities.

With this data model, the optimized sky recovery is described in a linear operation

$$\hat{\mathbf{m}}_{f_i} = \mathbf{D}_{f_i} \mathbf{A}_{f_i}^\dagger \mathbf{N}_{f_i}^{-1} \mathbf{d}_{f_i}, \quad (4)$$

where  $\hat{\mathbf{m}}_{f_i}$  is the estimated sky map,  $\mathbf{D}_{f_i}$  is a normalization matrix, and  $\mathbf{N}_{f_i}$  is the noise covariance matrix calculated as  $\mathbf{N}_{f_i} = \langle \mathbf{n}_{f_i}^\dagger \mathbf{n}_{f_i} \rangle_n$ . The  $\langle \dots \rangle_n$  operator means that we are averaging over different visibility noise realizations. Combining the above two equations, we define the point spread function (PSF) matrix  $\mathbf{P}_{f_i}$

$$\begin{aligned} \langle \hat{\mathbf{m}}_{f_i} \rangle_n &= \mathbf{D}_{f_i} \mathbf{A}_{f_i}^\dagger \mathbf{N}_{f_i}^{-1} (\mathbf{A}_{f_i} \mathbf{m}_{f_i} + \langle \mathbf{n}_{f_i} \rangle_n) \\ &= (\mathbf{D}_{f_i} \mathbf{A}_{f_i}^\dagger \mathbf{N}_{f_i}^{-1} \mathbf{A}_{f_i}) \mathbf{m}_{f_i} \\ &\equiv \mathbf{P}_{f_i} \mathbf{m}_{f_i}, \end{aligned} \quad (5)$$

where we use the property that noise averages to zero ( $\langle \mathbf{n}_{f_i} \rangle_n = 0$ ) in the above derivation, and the last line defines the PSF matrix as  $\mathbf{P}_{f_i} = \mathbf{D}_{f_i} \mathbf{A}_{f_i}^\dagger \mathbf{N}_{f_i}^{-1} \mathbf{A}_{f_i}$ . The map pixels are chosen to be smaller than the synthesized beam to ensure that the measurement resolution is limited by the instrument. The subscript  $f_i$  in all the variables indicates that they are for one frequency channel. Sky images are generated for each frequency channel, and frequency channels are converted into LOS distances. Combining the 2D sky images at different LOS distances yields a 3D image cube —  $\hat{\mathbf{m}}$ . It is related to the true 3D image cube  $\mathbf{m}$  by the 3D PSF matrix  $\mathbf{P}$ . We aggregate the 2D image PSF matrix  $\mathbf{P}_{f_i}$  to form the 3D PSF matrix with  $\mathbf{P}_{f_i}$  as block-diagonal matrices

$$\mathbf{P} = \text{diag}(\mathbf{P}_{f_1}, \dots, \mathbf{P}_{f_i}, \dots, \mathbf{P}_{f_N}). \quad (6)$$

Here we do not consider frequency-frequency correlations. The aggregated  $\mathbf{P}$  maps the true 3D image cube to the estimation

$$\langle \hat{\mathbf{m}} \rangle_n = \mathbf{P} \mathbf{m}, \quad (7)$$

where the 3D image cube  $\mathbf{m}$  and its estimation  $\hat{\mathbf{m}}$  are flattened to column vectors.

The image cube estimation is then tapered along the three dimensions. The tapering apodizes hard boundaries, suppressing ringing in Fourier space. Meanwhile, we treat all the power within each voxel as a single point source (Liu & Tegmark 2011; Dillon et al. 2013), and we will correct for the voxel window function later. With the Fourier Transform convention in Equation 1 and 2, we define the quadratic estimator of the image cube to be

$$\hat{q}_\alpha = \frac{V}{N^2} \hat{\mathbf{m}}^\dagger \mathbf{R}^\dagger \mathbf{E}_\alpha \mathbf{R} \hat{\mathbf{m}}, \quad (8)$$

where  $\mathbf{R}$  is the 3D tapering function of the image cube. Then, we define

$$\mathbf{E}_\alpha = \mathbf{c}_\alpha^\dagger \mathbf{c}_\alpha, \quad (9)$$

where  $\mathbf{c}_\alpha$  is the 3D discrete Fourier Transform operator at  $\mathbf{k}_\alpha$

$$\mathbf{c}_\alpha = (e^{-i\mathbf{k}_\alpha \cdot \mathbf{r}_1}, \dots, e^{-i\mathbf{k}_\alpha \cdot \mathbf{r}_j}, \dots, e^{-i\mathbf{k}_\alpha \cdot \mathbf{r}_N}). \quad (10)$$

Elements within  $\mathbf{c}_\alpha$  cover all voxels  $\mathbf{r}_i$  within the image cube; multiplying  $\mathbf{c}_\alpha$  on an image cube vector gives the Fourier Transform of the image cube at  $\mathbf{k}_\alpha$ . On the contrary, the conjugate transpose operator  $\mathbf{c}_\alpha^\dagger$  is the inverse 3D discrete Fourier Transform

$$\mathbf{c}_\alpha^\dagger = (e^{i\mathbf{k}_\alpha \cdot \mathbf{r}_1}, \dots, e^{i\mathbf{k}_\alpha \cdot \mathbf{r}_j}, \dots, e^{i\mathbf{k}_\alpha \cdot \mathbf{r}_N})^T. \quad (11)$$

Neither  $\mathbf{c}_\alpha$  nor  $\mathbf{c}_\alpha^\dagger$  contains DFT normalization factors; instead, the normalization factors are explicitly represented in the leading factors of Equation 8.

Coming back to the quadratic estimator  $\hat{q}_\alpha$ , plugging in the  $\mathbf{m}$  and  $\hat{\mathbf{m}}$  relation of Equation 7, the quadratic estimator is written as

$$\langle \hat{q}_\alpha \rangle_n = \frac{V}{N^2} \mathbf{m}^\dagger \mathbf{P}^\dagger \mathbf{R}^\dagger \mathbf{E}_\alpha \mathbf{R} \mathbf{P} \mathbf{m}. \quad (12)$$

With the true sky brightness, we define the voxel covariance  $\mathbf{C} \equiv \langle \mathbf{m} \mathbf{m}^\dagger \rangle$ . The  $\langle \dots \rangle$  operator indicates we are averaging over different sky realization, as initially defined in Equation 2. This covariance matrix is associated with the power spectrum, and can be expressed as a linear combination of the band powers (Dillon et al. 2013; Liu & Shaw 2020)

$$\mathbf{C} \equiv \langle \mathbf{m} \mathbf{m}^\dagger \rangle = \frac{1}{V} \sum_\beta p_\beta \mathbf{E}_\beta \cdot |\Phi(\mathbf{k}_\beta)|^2, \quad (13)$$

The above equation adds band powers across the  $\mathbf{k}$ -space, and the normalization factor  $1/V$  is the  $\mathbf{k}$ -space resolution for the summation. In addition, the  $\Phi(\mathbf{k}_\beta)$  function is the voxel window function at the  $\mathbf{k}_\beta$  position. We use the 3D boxcar profile as the real-space

voxel profile, therefore,  $\Phi(\mathbf{k}_\beta)$  is expressed as the product of three sinc functions:

$$\Phi(\mathbf{k}) \equiv j_0\left(\frac{k_x \Delta x}{2}\right) j_0\left(\frac{k_y \Delta y}{2}\right) j_0\left(\frac{k_z \Delta z}{2}\right), \quad (14)$$

where  $j_0(x) = \sin(x)/x$ ,  $k_x, k_y, k_z$  are the three components of the  $\mathbf{k}$  vector, and  $\Delta x, \Delta y, \Delta z$  are the real-space resolution of the image cube for each dimension (Dillon et al. 2013).

Equation 12 has scalars on both sides, so we add the trace operator on both sides. With the cyclic property of the trace, we can circularly shift the matrices on the right-hand side. Also using the above equation, we rewrite Equation 12

$$\begin{aligned} \langle \hat{q}_\alpha \rangle &= \frac{V}{N^2} \text{tr}[\langle \mathbf{m}^\dagger \mathbf{P}^\dagger \mathbf{R}^\dagger \mathbf{E}_\alpha \mathbf{R} \mathbf{P} \mathbf{m} \rangle] \\ &= \frac{V}{N^2} \text{tr}[\mathbf{P}^\dagger \mathbf{R}^\dagger \mathbf{E}_\alpha \mathbf{R} \mathbf{P} \langle \mathbf{m} \mathbf{m}^\dagger \rangle] \\ &= \frac{V}{N^2} \text{tr}[\mathbf{P}^\dagger \mathbf{R}^\dagger \mathbf{E}_\alpha \mathbf{R} \mathbf{P} \frac{1}{V} \sum_\beta p_\beta \mathbf{E}_\beta |\Phi(\mathbf{k}_\beta)|^2] \\ &= \frac{1}{N^2} \sum_\beta \text{tr}[\mathbf{P}^\dagger \mathbf{R}^\dagger \mathbf{E}_\alpha \mathbf{R} \mathbf{P} \mathbf{E}_\beta |\Phi(\mathbf{k}_\beta)|^2] p_\beta \\ &\equiv \sum_\beta H_{\alpha\beta} p_\beta. \end{aligned} \quad (15)$$

Please note that we are averaging over both noise realizations and sky realizations above. Here we define the power spectrum response function  $\mathbf{H}$ , which transfer the true sky power to our quadratic estimator. Element-wise,  $\mathbf{H}$  is written as

$$\begin{aligned} H_{\alpha\beta} &= \frac{|\Phi(\mathbf{k}_\beta)|^2}{N^2} \text{tr}(\mathbf{P}^\dagger \mathbf{R}^\dagger \mathbf{E}_\alpha \mathbf{R} \mathbf{P} \mathbf{E}_\beta) \\ &= \frac{|\Phi(\mathbf{k}_\beta)|^2}{N^2} \text{tr}(\mathbf{P}^\dagger \mathbf{R}^\dagger \mathbf{c}_\alpha^\dagger \mathbf{c}_\alpha \mathbf{R} \mathbf{P} \mathbf{c}_\beta^\dagger \mathbf{c}_\beta). \end{aligned} \quad (16)$$

Using the matrix trace cyclic property again, we can rewrite the above equation

$$\begin{aligned} H_{\alpha\beta} &= \frac{|\Phi(\mathbf{k}_\beta)|^2}{N^2} \text{tr}(\mathbf{c}_\beta \mathbf{P}^\dagger \mathbf{R}^\dagger \mathbf{c}_\alpha^\dagger \mathbf{c}_\alpha \mathbf{R} \mathbf{P} \mathbf{c}_\beta^\dagger) \\ &= \frac{|\Phi(\mathbf{k}_\beta)|^2}{N^2} \text{tr}[(\mathbf{c}_\alpha \mathbf{R} \mathbf{P} \mathbf{c}_\beta^\dagger)^\dagger (\mathbf{c}_\alpha \mathbf{R} \mathbf{P} \mathbf{c}_\beta^\dagger)] \\ &= |\Phi(\mathbf{k}_\beta)|^2 \text{tr}[(\frac{\mathbf{c}_\alpha}{\sqrt{N}} \mathbf{R} \mathbf{P} \frac{\mathbf{c}_\beta^\dagger}{\sqrt{N}})^\dagger (\frac{\mathbf{c}_\alpha}{\sqrt{N}} \mathbf{R} \mathbf{P} \frac{\mathbf{c}_\beta^\dagger}{\sqrt{N}})] \\ &= |\Phi(\mathbf{k}_\beta)|^2 |\frac{\mathbf{c}_\alpha}{\sqrt{N}} \mathbf{R} \mathbf{P} \frac{\mathbf{c}_\beta^\dagger}{\sqrt{N}}|^2, \end{aligned} \quad (17)$$

The last line indicates the normalization for DFT: we divide forward and background DFT by  $\sqrt{N}$ . Equation 17 is the formula to calculate the response matrix  $\mathbf{H}$ .

The  $\mathbf{H}$  matrix links the quadratic estimator  $\hat{\mathbf{q}}$  and the true power spectrum  $\mathbf{p}$  as

$$\langle \hat{\mathbf{q}} \rangle = \mathbf{H}\mathbf{p}. \quad (18)$$

The quadratic estimator  $\hat{\mathbf{q}}$  is an intermediate product of the power spectrum estimation, and we use the response matrix  $\mathbf{H}$  to convert it to the power spectrum estimator  $\hat{\mathbf{p}}$ . Equation 17 also shows that  $\mathbf{H}$  is determined by  $\mathbf{R}\mathbf{P}$  — the transfer function in image space. Essentially,  $\mathbf{H}$  and  $\mathbf{R}\mathbf{P}$  represent the same relation in two domains.

### 2.3. Window Functions

Window functions describe, in power spectrum space, how the true sky power is mapped into the measured power spectrum. Ideally, window functions are delta functions, which is not always achievable. In practice, one measured band power takes contribution from all parts of the true sky power. The contribution is characterized by a set of weights, which is the window function.

Continuing with Equation 18, if we could construct a matrix  $\mathbf{M}$  to invert  $\mathbf{H}$ , unambiguously recovering the underlining band power  $\mathbf{p}$  from  $\hat{\mathbf{q}}$ , we would equivalently obtain delta-function-like window functions. In practice,  $\mathbf{H}$  is generally not invertible for interferometers because of their incomplete  $uv$  coverage. Therefore, different forms of  $\mathbf{M}$  are constructed for various purposes (Seljak 1998; Tegmark et al. 2002; Liu & Tegmark 2011; Ali et al. 2015; HERA Collaboration et al. 2022; Kern & Liu 2021). Here we sum the columns for each row in the  $\mathbf{H}$  matrix and divide out the sum for each element in the corresponding row. Mathematically, we form a diagonal matrix  $\mathbf{M}$  with each element as the inverse of the row sum<sup>1</sup>

$$\mathbf{M} = \text{diag}\left(1/\sum_{\beta} H_{1,\beta}, \dots, 1/\sum_{\beta} H_{i,\beta}, \dots, 1/\sum_{\beta} H_{N,\beta}\right). \quad (19)$$

The full-rank  $\mathbf{M}$  matrix takes our quadratic estimator  $\hat{\mathbf{q}}$  to the estimated band powers  $\hat{\mathbf{p}}$  (Tegmark 1997; Liu et al. 2014)

$$\hat{\mathbf{p}} = \mathbf{M}\hat{\mathbf{q}}. \quad (20)$$

With this definition of  $\mathbf{M}$ , the window function matrix is defined as  $\mathbf{W} = \mathbf{M}\mathbf{H}$ , the normalized power is expressed as

$$\langle \hat{\mathbf{p}} \rangle = \mathbf{M}\langle \hat{\mathbf{q}} \rangle = \mathbf{M}\mathbf{H}\mathbf{p} = \mathbf{W}\mathbf{p}. \quad (21)$$

The window function matrix  $\mathbf{W}$  is fully defined by  $\mathbf{H}$

$$W_{\alpha\beta} = \sum_{\gamma} M_{\alpha\gamma} H_{\gamma\beta}$$

<sup>1</sup> Analogous to normalizing the weights for a weighted sum.

$$\begin{aligned} &= M_{\alpha\alpha} H_{\alpha\beta} \\ &= \frac{H_{\alpha\beta}}{\sum_{\delta} H_{\alpha\delta}}. \end{aligned} \quad (22)$$

The above equation also shows that weights in each row of  $\mathbf{W}$  sums to one. Despite being normalized, the weights' distribution varies across different power spectrum estimators. Accordingly, the measured power spectrum depends on the window function; we do not expect different power spectrum estimators to recover exactly the same power spectrum.

Window functions in the delay power spectrum were studied in Parsons et al. (2012); Liu et al. (2014); Gorcic et al. (2023); here, we investigate window functions from this image power spectrum.

## 3. IMAGE POWER SPECTRUM APPLICATION

Equipped with the above formalism, we investigate the properties of the image power spectrum. We map simulated noiseless visibilities to one image cube and calculate its image power spectrum along with the window functions. We compare the window functions with the delay spectrum ones to understand the difference between the two estimators. We show the 2D/1D power spectrum to evaluate the foreground separation.

### 3.1. The Image Cube

We use the HERA validation simulations (Aguirre et al. 2022), which is based on HERA Phase I array configuration with 33 unflagged antennas (HERA Collaboration et al. 2022, 2023). We choose three datasets with different sky models, including *EoR-only*, *foregrounds-only*, and *EoR+foregrounds*. Please note that the EoR signals in these simulations are boosted compared to the fiducial model (Aguirre et al. 2022). We employ these three variations to analyze their image power spectra. The simulation includes neither noise nor systematics. We select the data from one time-integration when the zenith is at 24.2° in R.A.; and we select a 17.5 MHz frequency range from 150.34 MHz to 167.84 MHz (with 0.098 MHz resolution). After Blackman-Harris tapering, the effective bandpass is around 8 MHz, within which cosmological evolution is insignificant. The frequency range and resolution are consistent with Band 2 defined in HERA Collaboration et al. (2022). The data contain both East-West and North-South polarization, we only analyze the East-West polarization in this paper.

We use the Fast Fourier Transform (FFT) algorithm to calculate the DFT, which requires a regular grid. Therefore, we create a regular R.A./Dec. grid in the sky-plane. However, the pixels do not have equal areas on a curved surface; their solid angle changes with the

pixel declination,

$$\Delta\Omega_{\text{px}} = \Delta\alpha\Delta\delta \cos(\delta), \quad (23)$$

where  $\alpha, \delta$  are R.A. and Dec.,  $\Delta\Omega$  is the pixel solid angle. From the above equation, we can see the pixel solid angle changes the slowest around  $\delta = 0$  since  $d\Delta\Omega_{\text{px}}/d\delta = \Delta\alpha\Delta\delta[-\sin(\delta)] = 0$  at  $\delta = 0$ . Therefore, we pixelize the sky with  $\delta = 0$  across the field center to minimize the pixel size change. This is equivalent to rotating the sky patch to the horizon for pixelization.

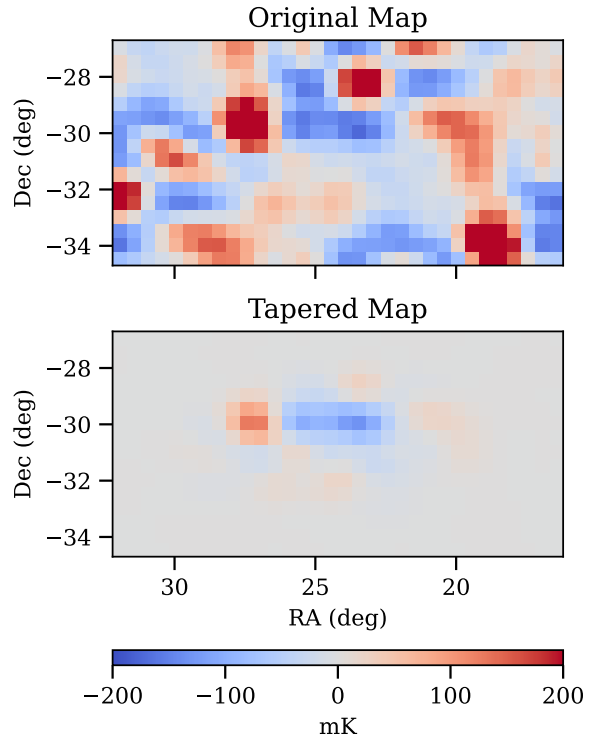
For each frequency channel, the visibilities are mapped with the direct optimal mapping algorithm. The grid is chosen to center at  $24.2^\circ$  in R.A. and  $-30.7^\circ$  in Dec., with  $0.5^\circ$  resolution along both directions. The  $0.5^\circ$  resolution is chosen to be half of the size of the  $\sim 1^\circ$  synthesized beam. The final map contains  $32 \times 16 = 512$  pixels, covering  $16^\circ \times 8^\circ = 128$  square degrees. The top panel of Figure 1 shows the map at the central frequency channel — 159.04 MHz. The mapping repeats for the 180 frequency channels.

The frequency channels are converted to redshifts and to comoving distances in the unit of  $\text{Mpc} \cdot \text{h}^{-1}$ . Uniform sampling in frequency leads to nonuniform sampling in comoving distances, because of the nonlinear relation between frequency and comoving distance. The distance intervals differ up to  $\sim 5.5\%$  across the whole range, we chose the average as the resolution along the LOS direction. In addition, comoving distances determine the physical spacing in the sky-plane. Within our frequency range, the comoving distance changes up to  $\sim 3.2\%$ ; we use the average LOS comoving distance to calculate the sky-plane resolution. Finally, the voxel size is calculated by multiplying the physical resolutions along three dimensions, which is  $\sim 3.5 \times 10^3 \text{Mpc}^3 \cdot \text{h}^{-3}$ . Table 1 collects the related parameters of the image cube. Please note the difference in comoving resolutions between the LOS and the sky-plane: the frequency channels provide much finer comoving resolution compared to the angular solution.

### 3.2. Window Function Results

Now we look at the image power spectrum window functions for the HERA Phase I configuration. Section 2.3 gives the theoretical formalism of the window function; here we present the actual calculation.

The aggregated  $\mathbf{P}$  matrix is a square matrix with  $(N_{\text{pixel}} \times N_{\text{freq}})^2 = (512 \times 180)^2 \approx 8 \times 10^9$  elements. Storing and operating this matrix is the most computationally expensive step in our image power spectrum analysis. The tapering matrix  $\mathbf{R}$  applies tapering functions along the three dimensions of the original image

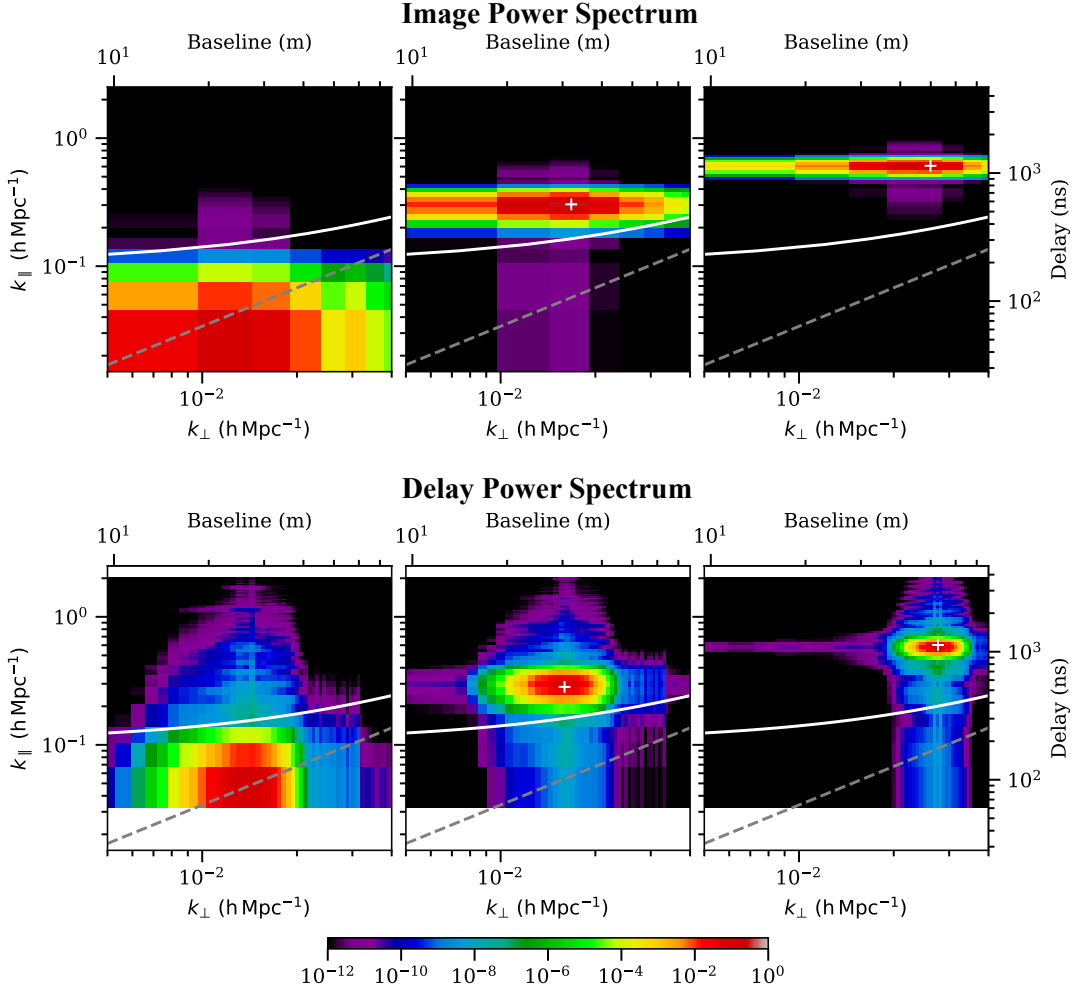


**Figure 1.** Original and tapered maps at 159.04 MHz. We use the direct optimal mapping algorithm (X22) to map the noiseless simulation data to regular R.A./Dec. grids. The original map consists of  $32 \times 16 = 512$  pixels, covering  $16^\circ \times 8^\circ = 128$  square degrees. After tapering with the Blackman-Harris function along three dimensions, the off-center signals are highly attenuated to suppress ringing structures from Fourier Transform. We select the center frequency for plotting where the frequency tapering effect is minimal. In total, we map 180 maps in the frequency range from 150.34 MHz to 167.84 MHz.

**Table 1.** Parameters for the Image Cube

Parameters	LOS	R.A.	Dec.
$N_{\text{pixel}}$	180	32	16
Range	17.5 MHz	$16^\circ$	$8^\circ$
Resolution	0.098 MHz	$0.5^\circ$	$0.5^\circ$
Range ( $\text{Mpc} \cdot \text{h}^{-1}$ )	205.4	1772	886
Resolution ( $\text{Mpc} \cdot \text{h}^{-1}$ )	1.21	55.4	55.4

NOTE—Image cube parameters shown in measurement units, including angular/frequency resolution, and the related comoving distances. We use the average comoving distance to calculate sky-plane resolution; we use the average LOS interval as the LOS resolution.



**Figure 2.** Window functions for image power spectrum and delay power spectrum. The top panels show image window functions at three  $(k_{\perp}, k_{\parallel})$  points; the bottom panels show delay window functions at similar  $(k_{\perp}, k_{\parallel})$  locations (Gorce et al. 2023). Locations of the native  $(k_{\perp}, k_{\parallel})$  bins are marked with white plus signs (the symbols are out of the plot range in the first column). All panels share the same logarithmic scales in two axes; they also share the same color range from 1 to  $10^{-12}$ . The dashed gray lines shows the horizon wedge and the solid white lines show 200 ns beyond the wedge. Both sets of window functions are based on the same array configuration and observation parameters. The  $k_{\perp} - k_{\parallel}$  binning is different from the image and delay power spectrum; white space is displayed where delay window functions do not have data. All the window functions are sum-normalized. The top and right axes show the corresponding baseline and delay values for  $k_{\perp}$  and  $k_{\parallel}$  respectively. The image window functions show lower power leakage along the  $k_{\parallel}$  direction ( $< 10^{-11}$ ) compared to the delay window functions, which is critical for foreground avoidance; the spread along the  $k_{\perp}$  direction is from the limited sky patch of the image cube.

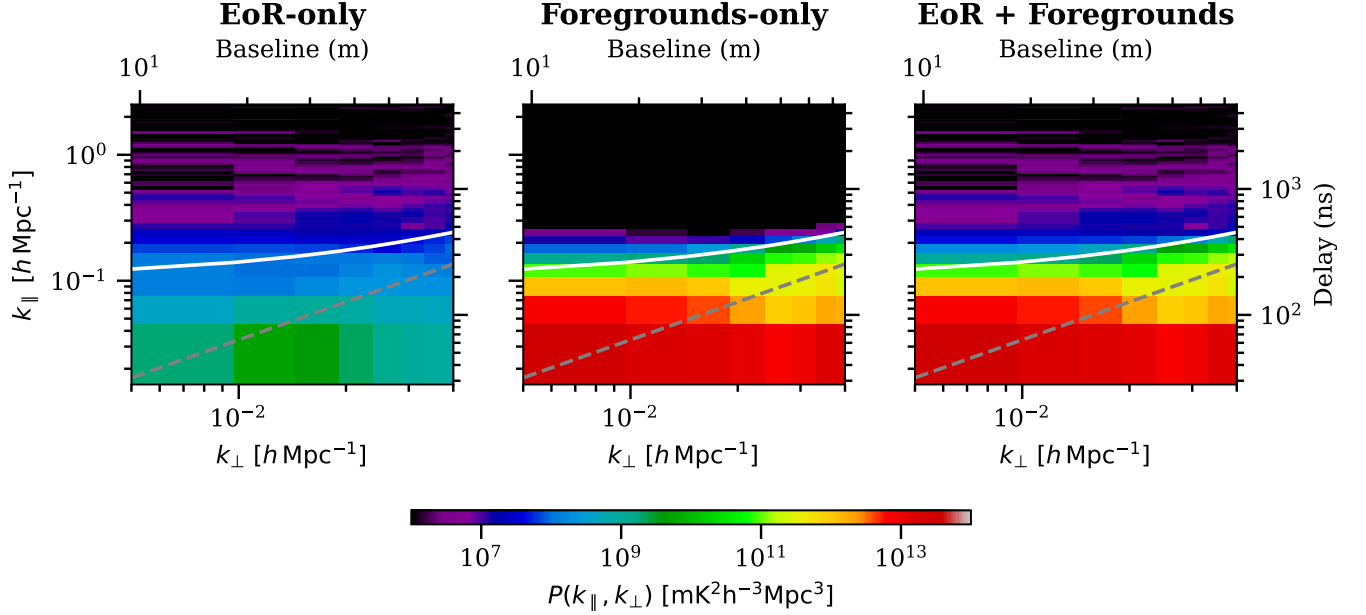
cube. Here we use the Blackman-Harris (4-term) tapering function along the three dimensions. A tapered map, perpendicular to LOS, is shown in the bottom panel of Figure 1.

To calculate  $\mathbf{H}$ , we pick individual columns in the  $\mathbf{RP}$  matrix, which are 3D vectors flattened to 1D. We reshape the 1D columns back into 3D and calculate their 3D FFT. The result is then flattened to replace the same column. The above process is repeated for all columns of  $\mathbf{RP}$ . Correspondingly, inverse FFT is performed across all rows from the previous result. Then, we square the individual elements of the matrix. Finally, we calculate

the pixel window function  $|\Phi(\mathbf{k})|^2$  and apply the result to all rows of the previous matrix to obtain  $\mathbf{H}$ .

Summing up columns in  $\mathbf{H}$ , we calculate the  $\mathbf{M}$  matrix according to Equation 19. The  $\mathbf{M}$  matrix normalizes the quadratic estimator to get the power spectrum estimator as in Equation 20. Finally, the window function matrix  $\mathbf{W}$  is calculated as  $\mathbf{W} = \mathbf{MH}$ . The window function matrix  $\mathbf{W}$  is defined in 3D band powers; for each  $\mathbf{k}$  bin, the corresponding window function shows the contribution from all the 3D  $\mathbf{k}$  bins. The dimension of the window functions can be reduced with symmetry, similar to the power spectrum. The two sky-plane





**Figure 3.** 2D image power spectra from EoR-only, foregrounds-only, and EoR+foregrounds simulations. The three power spectra were calculated from simulated visibilities. The power spectra share the same  $k_{\perp}$ ,  $k_{\parallel}$  range as well as the color range; the dashed line shows the horizon wedge and the solid line shows 200 ns beyond the wedge. The EoR power spectrum shows power distributed across the whole space, with more power at low- $k_{\parallel}$ . The foregrounds’ power is concentrated within low- $k_{\parallel}$  region, with an amplitude four orders of magnitude higher than that from the EoR power spectrum. However, there is a window not contaminated by the foregrounds in high- $k_{\perp}$  regions. Finally, the EoR+foregrounds power spectrum shows the result with both sky components: foreground features dominate low- $k_{\parallel}$  and EoR features prevail in the high- $k_{\parallel}$  EoR window.

dimensions are circularly binned into  $k_{\perp}$ ; the LOS direction is kept unchanged as  $k_{\parallel}$ . Values from related 3D  $\mathbf{k}$  bins are averaged into  $(k_{\perp}, k_{\parallel})$  space with equal weights. The  $k_{\parallel}$  direction is divided into 90 linear bins from 0 to  $2.71 \text{ h} \cdot \text{Mpc}^{-1}$ ; the  $k_{\perp}$  direction is divided into 16 linear bins from  $7.4 \times 10^{-3}$  to  $7.8 \times 10^{-2} \text{ h} \cdot \text{Mpc}^{-1}$ .

The top panels of Figure 2 show image power spectrum window functions at three  $(k_{\perp}, k_{\parallel})$  points. Along the  $k_{\perp}$  direction, the window functions show wide spreading. This is because we currently only consider a small sky patch as shown in Figure 1. The small sky patch and the sky-plane tapering functions generate the extended  $k_{\perp}$  kernels.

Along the  $k_{\parallel}$  direction, power leakage along the  $k_{\parallel}$  direction is suppressed below  $10^{-11}$ . This is critical for separating EoR from foregrounds: the smooth foregrounds only occupy low- $k_{\parallel}$  regions while the EoR signal takes up the entire  $k_{\perp} - k_{\parallel}$  space; therefore, the detectability of the EoR signal lies in the assumption that the foreground power can be contained only in low- $k_{\parallel}$  regions. The window functions in Figure 2 directly show how much power leaks from low- $k_{\parallel}$  to high- $k_{\parallel}$ .

The bottom panels of Figure 2 show window functions of the same datasets at similar  $(k_{\perp}, k_{\parallel})$  locations from the delay power spectrum (Gorce et al. 2023). In Gorce

et al. (2023), the same Blackman-Harris tapering is applied along the visibility frequency axis. The  $k_{\parallel}$  leakage is approximately three orders of magnitude higher than the image power spectrum, due to the spatial structures leaking into the frequency axis, as discussed in Section 2. However, along the  $k_{\perp}$  direction, the window functions display a more compact kernel compared to the image power spectrum. This is because visibilities integrate the whole sky and the delay spectrum analyzes visibilities directly, equivalently measuring the full sky weighted by the primary beam; compared to the small sky patch in the image power spectrum, the delay spectrum window functions show more compact kernels along  $k_{\perp}$ .

Because we cannot fully deconvolve the power spectrum response function, the measured power spectrum receives contributions across all  $\mathbf{k}$  bins from the true band powers, whose distribution is presented in window functions. The window functions show that the image and delay power spectrum are different estimators of the true sky band powers.

### 3.3. 2D Power Spectrum

The previous section examines the window functions from three representative  $(k_{\perp}, k_{\parallel})$  bins, now we investigate the full 2D image power spectra.

We first calculate the quadratic estimator  $\hat{\mathbf{q}}$  with Equation 8. We FFT and inverse FFT the tapered image cube and multiply the results together element-wise, then we multiply the  $V/N$  factor<sup>2</sup> to obtain the 3D quadratic estimator  $\hat{\mathbf{q}}$ . We use the matrix  $\mathbf{M}$  to normalize the quadratic estimator for the power spectrum estimator (Equation 20). After obtaining the normalized 3D power spectrum estimator, we bin it to the  $(k_{\perp}, k_{\parallel})$  space by averaging the related 3D band power. In the averaging step, we use equal weights. The power spectrum in the 2D  $(k_{\perp}, k_{\parallel})$  space are shown in Figure 3.

The EoR-only power spectrum shows power across the entire  $k_{\perp} - k_{\parallel}$  space. Not much change is observed along the  $k_{\perp}$  direction while there is a clear decreasing trend from low- $k_{\parallel}$  to high- $k_{\parallel}$ . The peak of the 2D power spectrum is around  $10^{10} \text{mK}^2 \cdot \text{h}^{-3} \text{Mpc}^3$ ; the amplitude is highly amplified in the simulation. The foregrounds-only power spectrum shows a different situation: the power is constrained within the low- $k_{\parallel}$  regions, mostly within 200 ns beyond the horizon wedge. The peak of the foregrounds-only power spectrum rises as high as  $10^{14} \text{mK}^2 \cdot \text{h}^{-3} \text{Mpc}^3$ , four orders of magnitude higher than the simulated EoR-only peak. However, its power does not leak into the high- $k_{\parallel}$  region with  $> 10^8$  dynamic range. This is consistent with the window function result above: the window functions show  $< 10^{-11}$  leakage from low- $k_{\parallel}$  to high- $k_{\parallel}$ , which ensures the overwhelming power from the smooth foregrounds does not affect the EoR window.

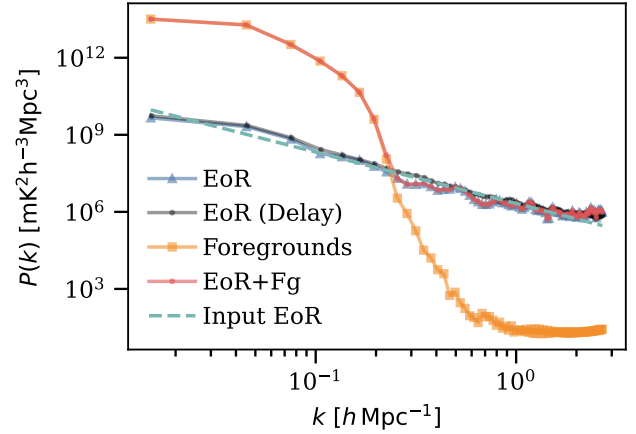
Finally, we come to the power spectrum of EoR+foregrounds. Please note that this power spectrum is not obtained by simply adding the previous two power spectra; instead, we start from visibilities, form the image cubes, and calculate the 2D power spectrum. In this power spectrum, the low- $k_{\parallel}$  region is dominated by the foregrounds, resembling the features in the foregrounds-only power spectrum; the high- $k_{\parallel}$  region is filled by EoR signals. The clear separation between the foregrounds and the EoR further illustrates the detectability of the EoR with the image power spectrum.

### 3.4. 1D Power Spectrum

The EoR power spectrum is often collapsed into 1D assuming it is homogeneous and isotropic.<sup>3</sup> We present the 1D power spectrum in this section by binning the original 3D power spectrum. The binning is based on

<sup>2</sup> The other  $N$  in the denominator is included in the FFT and iFFT normalization.

<sup>3</sup> Please refer to Section 2.1 for discussions on symmetry and power spectrum dimension reduction.



**Figure 4.** 1D power spectrum measured from three simulation datasets. The foreground signal dominates in the low- $k$  regions; the boosted EoR signal dominates in the high- $k$  region. Also shown is the EoR-only spectrum measured by the delay power spectrum. Both the image power spectrum and the delay power spectrum agree with the input power, represented in a dashed line. The deviation of the measurement at high- $k$  is due to aliasing from DFT (Aguirre et al. 2022). The deviation from a straight line in the mid- $k$  range is due to the small sky patch selected for the image power spectrum.

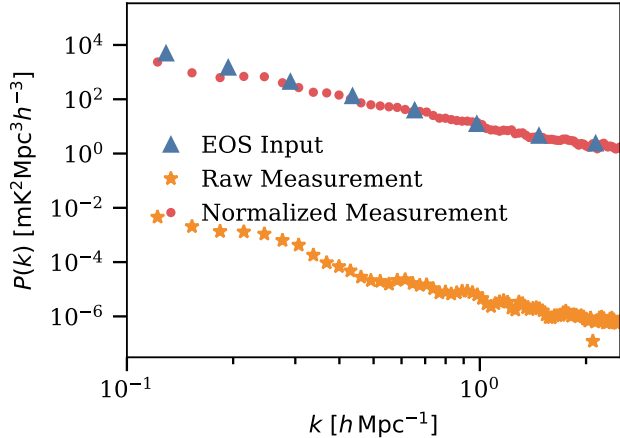
equal-weight averaging, similar to the 2D power spectrum.

Figure 4 shows the 1D power spectrum from EoR-only, foregrounds-only, and EoR+foregrounds simulations. The EoR+foregrounds 1D power spectrum closely follows the foregrounds-only spectrum in low- $k$  and the EoR-only spectrum in high- $k$ . In high- $k$ , the EoR signal is more than five orders of magnitude stronger than that of the foregrounds. The foreground avoidance capability of the image power spectrum is illustrated in this figure. Also plotted is the 1D EoR-only power spectrum measured with the delay power spectrum, and the input EoR power. The image power spectrum and delay power spectrum both recover the input EoR power.

In addition, we use the Evolution Of 21 cm Structure (EOS)<sup>4</sup> simulation (Sobacchi & Mesinger 2014) to further validate the image power spectrum 1D power spectrum. The EOS project provides image cubes and also their input 1D power spectrum. Therefore, we can calculate the 1D image power spectrum and compare it with the input.

The EOS simulation provides image cubes with 1.6 Gpc ( $1.11 \text{Gpc} \cdot \text{h}^{-1}$ ) and 1024 bins on each side. We use one image cube at redshift 5.76. Along the x-axis,

<sup>4</sup> URL: <http://homepage.sns.it/mesinger/EOS.html>



**Figure 5.** 1D Power Spectrum from the evolution of 21 cm structure (EOS) simulation. We downsample and convolve the EOS image cube and measure the 1D image power spectrum. The normalized 1D power spectrum agrees with the input after being adjusted by six orders of magnitude from the normalization step.

we downsample the EOS image cube into 32 bins; along the y-axis, we also downsample the EOS image cube into 32 bins but select the middle 16 bins; along the z-axis, we select the first 180 bins without downsampling. We average the intensity among associated voxels during downsampling. This gives us the  $180 \times 32 \times 16$  image cube similar to the DOM image cube. Then we convolve the downsampled EOS image cube with the  $\mathbf{P}$  matrix to get the instrument-convolved image cube.

We measure the image power spectrum and bin the 3D power spectrum into 1D. Figure 5 shows the input 1D power spectrum and the normalized 1D power spectrum from DOM. The measurement recovers the input 1D power spectrum across the majority of the  $k$ , with some mismatch at the low- $k$  end. The inconsistency at the low- $k$  end comes from the edge effect of the finite EOS image cube. The finite EOS image cube contains no power beyond its size, beyond the lower limit of  $k_{\perp}$ ; the window functions average down the power close to the  $k_{\perp}$  lower limit. Also shown in Figure 5 is the 1D power spectrum before normalization. The comparison shows the normalization correctly rescales the power spectrum over six orders of magnitude.

#### 4. COMPLETE UV-COVERAGE

The HERA array configuration does not have complete  $uv$  coverage (Dillon & Parsons 2016). The incomplete  $uv$  coverage comes with ambiguity in imaging; this is clearly demonstrated as grating lobes in the PSF (X22). The size and location of the grating lobes change with frequency, leaking spatial power into the

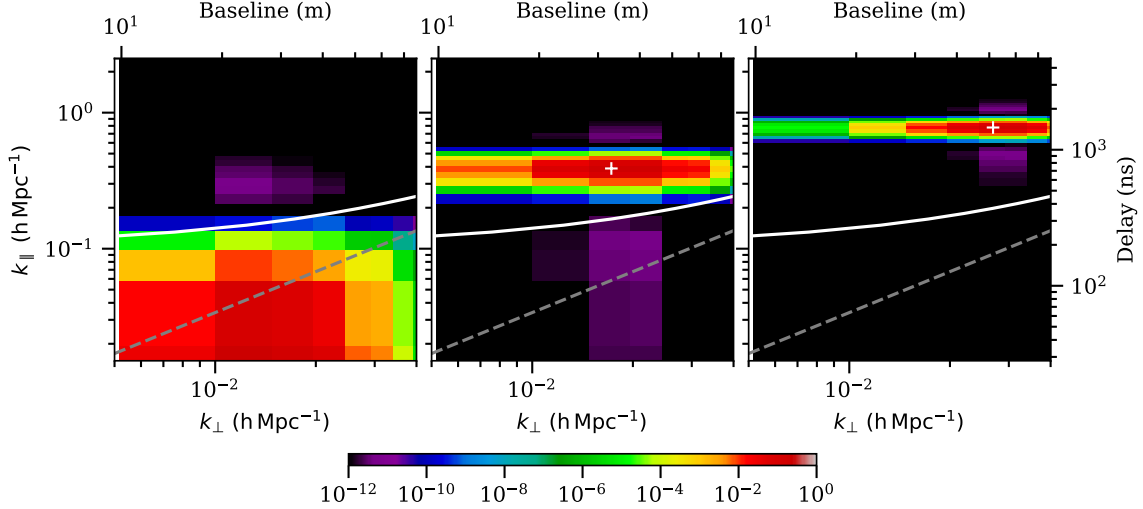
frequency axis. Therefore, with a  $uv$  incomplete array, we do not achieve the full advantage of the image power spectrum (Morales et al. 2019).

To evaluate how much improvement we can expect if we had complete  $uv$  coverage, we simulate visibilities from a  $uv$ -complete interferometer array with the `pyuvsim` package (Lanman et al. 2019). Using the average wavelength at 1.64 m as a reference, we first evenly divide half of the  $uv$  space from 10 to 100 wavelengths into one-wavelength cells. We then fill each cell with a baseline at a randomized location, giving us 15,604 visibilities in total. This setup represents an array with complete  $uv$  coverage from ten to one hundred wavelengths at the resolution of one wavelength — 1.64 m. The  $uv$  pattern is created at the reference wavelength and fixed in its physical size, so it evolves with frequency: both the  $uv$  coverage and resolution change across the frequency band. This  $uv$  pattern does not require any certain pairs of antennas located at one reference wavelength apart, because the  $uv$  coverage starts from 10 reference wavelengths. For example, antennas representing two close baselines can come from four antennas — two pairs — with each pair separated by at least 10 reference wavelengths; an array designed to cover these  $uv$  locations will have additional baselines beyond the ones in the simulation, we do not consider them for this study. Adding the additional baseline, equivalently adding additional information, will only improve the results from this study.

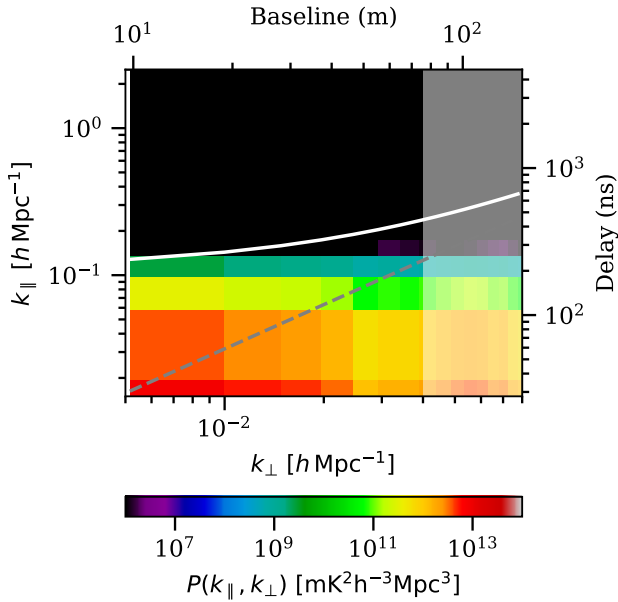
After adopting a 14-m Airy profile for the primary beam, we use a diffuse sky map (Byrne et al. 2022) and the GLEAM sources (Wayth et al. 2015; Hurley-Walker et al. 2017, 2019) to simulate the visibilities for one time-integration. During the integration, the array points at  $0^{\circ}$  R.A. and  $-26.7^{\circ}$  Dec. No noise or mitigated systematics is added to the visibilities.

We use direct optimal mapping to map the visibilities to one image cube; each sky image has the same range and resolution as the image cube in Section 3.1 except centering at the  $0^{\circ}$  R.A. and  $-26.7^{\circ}$  Dec. We select 180 channels closest to the frequency range in the previous analysis — 167.07 MHz to 181.40 MHz with a resolution of 0.08 MHz. Please note that the  $uv$ -complete simulation uses a different sky model, assumes a different primary beam model, centers on a different sky patch, and measures a different frequency range compared to the previous section; so the exact foreground map and power are different. However, we can still investigate how the foreground power is distributed in the 2D  $k_{\perp} - k_{\parallel}$  space.

After the image cube is formed, we use the image power spectrum pipeline to calculate its window functions and 2D power spectrum. Figure 6 shows window



**Figure 6.** Window functions for a  $uv$ -complete array. The three native  $k$  bins,  $k_{\perp}/k_{\parallel}$  range, and the color range are the same as in Figure 2. With the complete  $uv$  coverage, the power leakage from low  $k_{\parallel}$  regions is further suppressed by the improved  $uv$  coverage but not completely eliminated in the given color range. The spread along the  $k_{\perp}$  direction is also reduced from the complete  $uv$  coverage.



**Figure 7.** 2D power spectrum from a  $uv$ -complete array. The  $k_{\parallel}$  range and the color range are identical to the ones in Figure 3. However, the  $k_{\perp}$  range is extended given the enlarged  $uv$  coverage. The extended part in  $k_{\perp}$  is shaded. The horizon wedge is not present with the complete  $uv$  coverage, even after extending the  $k_{\perp}$  range. The  $uv$ -complete 2D power spectrum shows less power compared to the previous foregrounds+EoR simulation. This is expected because the  $uv$ -complete simulation assumes different sky models, points at a different sky patch, and covers a different frequency band.

functions at the three representative points as in Figure 2. Window functions with complete  $uv$ -coverage show less  $k_{\parallel}$ -leakage from the ones in Figure 2. However, we still see leakage along the  $k_{\parallel}$  at the  $10^{-12}$  level. We find the  $k_{\parallel}$  leakage disappears in the current color scale if we use a more aggressive tapering function — 7-term Blackman-Harris — along the LOS direction; in exchange, we get a larger kernel along  $k_{\parallel}$ .

Figure 7 shows the 2D power spectrum similar to the ones in Figure 3. The  $uv$ -complete 2D power spectrum extends farther out along the  $k_{\perp}$  direction, thanks to the array’s larger  $uv$  range; for comparison, the extended part is shaded in Figure 7. The horizon wedge is generally more prominent in high- $k_{\perp}$ , so extending  $k_{\perp}$  should reveal more of the horizon wedge. We start to see the horizon wedge in Figure 3 with the HERA array; however, even after extending to higher  $k_{\perp}$  values, we do not see the wedge in Figure 7 with the  $uv$ -complete array. This delivers an interesting message: image power spectrum from a  $uv$ -complete array does not see the horizon wedge.

This study decouples the effect from a  $uv$ -incomplete array and the intrinsic properties from the image power spectrum. For an array with complete  $uv$  coverage, we achieve the full potential of the image power spectrum, with the 2D power spectrum showing a mitigated horizon wedge, which is our initial motivation to develop the image power spectrum; here we quantitatively verified this conclusion with end-to-end simulation and analysis. Now, two caveats are worth mentioning: we assumed a 14-m Airy beam in this study, without considering the complexity of realistic primary beams (Kim et al. 2022,

2023); we did not simulate noise, instrument systematics, or calibration errors, which can introduce the wedge even in image power spectra (Morales et al. 2019).

Murray & Trott (2018) conducted an investigation of different array layouts, and concluded that radially randomized arrays show the wedge feature in the 2D power spectrum. The power spectrum estimator in Murray & Trott (2018) is based on  $uv$ -mapping, different from the image power spectrum in this paper.

## 5. FUTURE WORK

We have developed the image power spectrum pipeline and understand its window function and power spectra with noiseless simulations. We will investigate the effects of realistic noise, radio-frequency interference, realistic errors in beam models (Kim et al. 2022, 2023), calibration accuracy, realistic antenna position, and beam variations (Orosz et al. 2019; Aguirre et al. 2022). We plan to apply this method on the HERA Phase I data (HERA Collaboration et al. 2022, 2023). The image power spectrum provides an independent statistic of the sky in addition to the delay power spectrum (HERA Collaboration et al. 2022, 2023).

Currently, we map only 512 pixels on the sky plane, limited by the size of the  $\mathbf{P}$  matrix and the calculation of the window function. After understanding the window function, we do not need to calculate its full form; instead, we only need the sum of each  $\mathbf{k}$  bin for normalization, which will dramatically reduce the RAM requirement of calculation. The reduction will enable us to increase the size and resolution of the image cube, enlarging the  $k_{\perp}$  range. With an enlarged sky patch, we can include more data at different local sidereal times (LSTs); we leave these topics for future work.

## 6. CONCLUSION

The image power spectrum measures  $k_{\parallel}$  directly through sky pixels, mitigating spatial power leaking into the frequency axis through measuring visibilities. This paper presents an FFT-based image power spectrum based on the direct optimal mapping (X22).

We use noiseless simulation data from Aguirre et al. (2022) to explore the image power spectrum. After obtaining the image cube with direct optimal mapping, the image cube is tapered along the three axes before performing a 3D FFT to calculate the power spectrum. We calculate the normalization factors for the power spectrum and the power spectrum window functions. The window functions show  $< 10^{-11}$  leakage along the  $k_{\parallel}$  direction, separating the foreground from EoR signals. The 2D and 1D power spectra also show that the EoR and foreground signals are clearly separated in  $\mathbf{k}$  space.

However, we still see the horizon wedge in the 2D power spectrum.

To understand whether the wedge feature comes from the image power spectrum or from HERA’s incomplete  $uv$  coverage, we simulated visibilities from a  $uv$ -complete array and analyzed the visibilities with our image power spectrum pipeline. For the window functions, leakage along the  $k_{\parallel}$  direction is less than  $10^{-12}$ , currently dominated by the tapering function’s dynamic range; the 2D power spectrum does not show wedge features either, even after extending the  $k_{\perp}$  range. This study highlights the potential utility of complete  $uv$ -coverage when evaluating future array designs: a  $uv$ -complete array, which contains complete information for imaging, does not show the horizon wedge in 2D image power spectra.

We plan to measure the image power spectrum using HERA data (DeBoer et al. 2017; HERA Collaboration et al. 2022, 2023). The result will provide a measurement that complements the delay spectrum, with different foreground features in the 2D power spectrum.

## ACKNOWLEDGEMENTS

This analysis utilized custom-built, publicly-accessible software by the HERA Collaboration (<https://github.com/Hera-Team>) in addition to software built by both HERA members and collaborators (<https://github.com/RadioAstronomySoftwareGroup>), especially `pyuvdata` (Hazelton et al. 2017). This analysis also relied on number of public, open-source software packages, including `numpy` (Harris et al. 2020), `scipy` (Virtanen et al. 2020), `matplotlib` (Hunter 2007), and `astropy` (Astropy Collaboration et al. 2018).

This material is based upon work supported by the National Science Foundation under grants #1636646 and #1836019 and institutional support from the HERA collaboration partners. This research is funded in part by the Gordon and Betty Moore Foundation through Grant GBMF5212 to the Massachusetts Institute of Technology. HERA is hosted by the South African Radio Astronomy Observatory, which is a facility of the National Research Foundation, an agency of the Department of Science and Innovation.

We acknowledge the use of the Ilifu cloud computing facility ([www.ilifu.ac.za](http://www.ilifu.ac.za)) and the support from the Inter-University Institute for Data Intensive Astronomy (IDIA; <https://www.idia.ac.za>).

J.S. Dillon gratefully acknowledges the support of the NSF AAPF award #1701536. NK acknowledges support from NASA through the NASA Hubble Fellowship grant #HST-HF2-51533.001-A awarded by the Space Telescope Science Institute, which is operated by

the Association of Universities for Research in Astronomy, Incorporated, under NASA contract NAS5-26555. R. Byrne is supported by National Science Foundation Award No. 2303952. P. Kittiwisit and M.G. Santos acknowledge support from the South African Radio Astronomy Observatory (SARAO; [www.sarao.ac.za](http://www.sarao.ac.za)) and the National Research Foundation (Grant No. 84156). This result is part of a project that has received funding from the European Research Council (ERC) under the European Union’s Horizon 2020 research and innovation programme (Grant agreement No. 948764; P. Bull and M.J. Wilensky). P. Bull and H. Garsden acknowledge support from STFC Grant ST/T000341/1. Parts of this research were supported by the Australian Research Council Centre of Excellence for All Sky Astrophysics in 3 Dimensions (ASTRO 3D), through project number CE170100013. G. Bernardi acknowledges funding from the INAF PRIN-SKA 2017 project 1.05.01.88.04 (FORECaST), support from the Ministero degli Af-

fari Esteri della Cooperazione Internazionale – Direzione Generale per la Promozione del Sistema Paese Progetto di Grande Rilevanza ZA18GR02 and the National Research Foundation of South Africa (Grant Number 113121) as part of the ISARP RADIOSKY2020 Joint Research Scheme, from the Royal Society and the Newton Fund under grant NA150184 and from the National Research Foundation of South Africa (grant No. 103424). E. de Lera Acedo acknowledges the funding support of the UKRI Science and Technology Facilities Council SKA grant. A. Liu acknowledges support from the New Frontiers in Research Fund Exploration grant program, the Canadian Institute for Advanced Research (CIFAR) Azrieli Global Scholars program, a Natural Sciences and Engineering Research Council of Canada (NSERC) Discovery Grant and a Discovery Launch Supplement, the Sloan Research Fellowship, and the William Dawson Scholarship at McGill.

## REFERENCES

- Abbott, T. M. C., Agüena, M., Alarcon, A., et al. 2022, *PhRvD*, 105, 023520, doi: [10.1103/PhysRevD.105.023520](https://doi.org/10.1103/PhysRevD.105.023520)
- Aguirre, J. E., Murray, S. G., Pascua, R., et al. 2022, *ApJ*, 924, 85, doi: [10.3847/1538-4357/ac32cd](https://doi.org/10.3847/1538-4357/ac32cd)
- Alam, S., Ata, M., Bailey, S., et al. 2017, *MNRAS*, 470, 2617, doi: [10.1093/mnras/stx721](https://doi.org/10.1093/mnras/stx721)
- Ali, Z. S., Parsons, A. R., Zheng, H., et al. 2015, *ApJ*, 809, 61, doi: [10.1088/0004-637X/809/1/61](https://doi.org/10.1088/0004-637X/809/1/61)
- Anderson, L., Aubourg, É., Bailey, S., et al. 2014, *MNRAS*, 441, 24, doi: [10.1093/mnras/stu523](https://doi.org/10.1093/mnras/stu523)
- Astropy Collaboration, Price-Whelan, A. M., SipHocz, B. M., et al. 2018, *AJ*, 156, 123, doi: [10.3847/1538-3881/aabc4f](https://doi.org/10.3847/1538-3881/aabc4f)
- Barry, N., Beardsley, A. P., Byrne, R., et al. 2019, *PASA*, 36, e026, doi: [10.1017/pasa.2019.21](https://doi.org/10.1017/pasa.2019.21)
- Beardsley, A. P., Hazelton, B. J., Sullivan, I. S., et al. 2016, *ApJ*, 833, 102, doi: [10.3847/1538-4357/833/1/102](https://doi.org/10.3847/1538-4357/833/1/102)
- Bennett, C. L., Banday, A. J., Gorski, K. M., et al. 1996, *ApJL*, 464, L1, doi: [10.1086/310075](https://doi.org/10.1086/310075)
- Bennett, C. L., Larson, D., Weiland, J. L., et al. 2013, *ApJS*, 208, 20, doi: [10.1088/0067-0049/208/2/20](https://doi.org/10.1088/0067-0049/208/2/20)
- Byrne, R., Morales, M. F., Hazelton, B., et al. 2022, *MNRAS*, 510, 2011, doi: [10.1093/mnras/stab3276](https://doi.org/10.1093/mnras/stab3276)
- Clark, B. G. 1980, *A&A*, 89, 377
- Cornwell, T. J. 2008, *IEEE Journal of Selected Topics in Signal Processing*, 2, 793, doi: [10.1109/JSTSP.2008.2006388](https://doi.org/10.1109/JSTSP.2008.2006388)
- Datta, A., Bowman, J. D., & Carilli, C. L. 2010, *ApJ*, 724, 526, doi: [10.1088/0004-637X/724/1/526](https://doi.org/10.1088/0004-637X/724/1/526)
- DeBoer, D. R., Parsons, A. R., Aguirre, J. E., et al. 2017, *PASP*, 129, 045001, doi: [10.1088/1538-3873/129/974/045001](https://doi.org/10.1088/1538-3873/129/974/045001)
- Dillon, J. S., Liu, A., & Tegmark, M. 2013, *PhRvD*, 87, 043005, doi: [10.1103/PhysRevD.87.043005](https://doi.org/10.1103/PhysRevD.87.043005)
- Dillon, J. S., & Parsons, A. R. 2016, *ApJ*, 826, 181, doi: [10.3847/0004-637X/826/2/181](https://doi.org/10.3847/0004-637X/826/2/181)
- Dillon, J. S., Liu, A., Williams, C. L., et al. 2014, *PhRvD*, 89, 023002, doi: [10.1103/PhysRevD.89.023002](https://doi.org/10.1103/PhysRevD.89.023002)
- Dillon, J. S., Neben, A. R., Hewitt, J. N., et al. 2015, *PhRvD*, 91, 123011, doi: [10.1103/PhysRevD.91.123011](https://doi.org/10.1103/PhysRevD.91.123011)
- Ewall-Wice, A., Dillon, J. S., Hewitt, J. N., et al. 2016, *MNRAS*, 460, 4320, doi: [10.1093/mnras/stw1022](https://doi.org/10.1093/mnras/stw1022)
- Fixsen, D. J., Cheng, E. S., Gales, J. M., et al. 1996, *ApJ*, 473, 576, doi: [10.1086/178173](https://doi.org/10.1086/178173)
- Furlanetto, S. R., Oh, S. P., & Briggs, F. H. 2006, *PhR*, 433, 181, doi: [10.1016/j.physrep.2006.08.002](https://doi.org/10.1016/j.physrep.2006.08.002)
- Gorce, A., Ganjam, S., Liu, A., et al. 2023, *MNRAS*, 520, 375, doi: [10.1093/mnras/stad090](https://doi.org/10.1093/mnras/stad090)
- Greig, B., Mesinger, A., & Pober, J. C. 2016, *MNRAS*, 455, 4295, doi: [10.1093/mnras/stv2618](https://doi.org/10.1093/mnras/stv2618)
- Harris, C. R., Millman, K. J., van der Walt, S. J., et al. 2020, *Nature*, 585, 357362, doi: [10.1038/s41586-020-2649-2](https://doi.org/10.1038/s41586-020-2649-2)
- Hazelton, B. J., Jacobs, D. C., Pober, J. C., & Beardsley, A. P. 2017, *The Journal of Open Source Software*, 2, 140, doi: [10.21105/joss.00140](https://doi.org/10.21105/joss.00140)
- HERA Collaboration, Abdurashidova, Z., Aguirre, J. E., et al. 2022, *ApJ*, 925, 221, doi: [10.3847/1538-4357/ac1c78](https://doi.org/10.3847/1538-4357/ac1c78)

- HERA Collaboration, Abdurashidova, Z., Adams, T., et al. 2023, *The Astrophysical Journal*, 945, 124, doi: [10.3847/1538-4357/acaf50](https://doi.org/10.3847/1538-4357/acaf50)
- Hinshaw, G., Larson, D., Komatsu, E., et al. 2013, *ApJS*, 208, 19, doi: [10.1088/0067-0049/208/2/19](https://doi.org/10.1088/0067-0049/208/2/19)
- Hogan, C. J., & Rees, M. J. 1979, *MNRAS*, 188, 791, doi: [10.1093/mnras/188.4.791](https://doi.org/10.1093/mnras/188.4.791)
- Högbom, J. A. 1974, *A&AS*, 15, 417
- Hu, W., & Dodelson, S. 2002, *ARA&A*, 40, 171, doi: [10.1146/annurev.astro.40.060401.093926](https://doi.org/10.1146/annurev.astro.40.060401.093926)
- Hunter, J. D. 2007, *Computing in Science & Engineering*, 9, 90, doi: [10.1109/MCSE.2007.55](https://doi.org/10.1109/MCSE.2007.55)
- Hurley-Walker, N., Callingham, J. R., Hancock, P. J., et al. 2017, *MNRAS*, 464, 1146, doi: [10.1093/mnras/stw2337](https://doi.org/10.1093/mnras/stw2337)
- Hurley-Walker, N., Hancock, P. J., Franzen, T. M. O., et al. 2019, *PASA*, 36, e047, doi: [10.1017/pasa.2019.37](https://doi.org/10.1017/pasa.2019.37)
- Kern, N. S., & Liu, A. 2021, *MNRAS*, 501, 1463, doi: [10.1093/mnras/staa3736](https://doi.org/10.1093/mnras/staa3736)
- Kern, N. S., Liu, A., Parsons, A. R., Mesinger, A., & Greig, B. 2017, *ApJ*, 848, 23, doi: [10.3847/1538-4357/aa8bb4](https://doi.org/10.3847/1538-4357/aa8bb4)
- Kim, H., Nhan, B. D., Hewitt, J. N., et al. 2022, *ApJ*, 941, 207, doi: [10.3847/1538-4357/ac9eaf](https://doi.org/10.3847/1538-4357/ac9eaf)
- Kim, H., Kern, N. S., Hewitt, J. N., et al. 2023, *ApJ*, 953, 136, doi: [10.3847/1538-4357/ace35e](https://doi.org/10.3847/1538-4357/ace35e)
- Lanman, A., Hazelton, B., Jacobs, D., et al. 2019, *The Journal of Open Source Software*, 4, 1234, doi: [10.21105/joss.01234](https://doi.org/10.21105/joss.01234)
- Li, W., Pober, J. C., Barry, N., et al. 2019, *ApJ*, 887, 141, doi: [10.3847/1538-4357/ab55e4](https://doi.org/10.3847/1538-4357/ab55e4)
- Liu, A., Parsons, A. R., & Trott, C. M. 2014, *PhRvD*, 90, 023018, doi: [10.1103/PhysRevD.90.023018](https://doi.org/10.1103/PhysRevD.90.023018)
- Liu, A., Parsons, A. R., & Trott, C. M. 2014, *Phys. Rev. D*, 90, 023019, doi: [10.1103/PhysRevD.90.023019](https://doi.org/10.1103/PhysRevD.90.023019)
- Liu, A., & Shaw, J. R. 2020, *PASP*, 132, 062001, doi: [10.1088/1538-3873/ab5bfd](https://doi.org/10.1088/1538-3873/ab5bfd)
- Liu, A., & Tegmark, M. 2011, *PhRvD*, 83, 103006, doi: [10.1103/PhysRevD.83.103006](https://doi.org/10.1103/PhysRevD.83.103006)
- Madau, P., Meiksin, A., & Rees, M. J. 1997, *ApJ*, 475, 429, doi: [10.1086/303549](https://doi.org/10.1086/303549)
- Mao, Y., Tegmark, M., McQuinn, M., Zaldarriaga, M., & Zahn, O. 2008, *PhRvD*, 78, 023529, doi: [10.1103/PhysRevD.78.023529](https://doi.org/10.1103/PhysRevD.78.023529)
- Mesinger, A., & Furlanetto, S. 2007, *ApJ*, 669, 663, doi: [10.1086/521806](https://doi.org/10.1086/521806)
- Morales, M. F., Beardsley, A., Pober, J., et al. 2019, *MNRAS*, 483, 2207, doi: [10.1093/mnras/sty2844](https://doi.org/10.1093/mnras/sty2844)
- Morales, M. F., Hazelton, B., Sullivan, I., & Beardsley, A. 2012, *ApJ*, 752, 137, doi: [10.1088/0004-637X/752/2/137](https://doi.org/10.1088/0004-637X/752/2/137)
- Morales, M. F., & Hewitt, J. 2004, *ApJ*, 615, 7, doi: [10.1086/424437](https://doi.org/10.1086/424437)
- Morales, M. F., & Wyithe, J. S. B. 2010, *ARA&A*, 48, 127, doi: [10.1146/annurev-astro-081309-130936](https://doi.org/10.1146/annurev-astro-081309-130936)
- More, S., Sugiyama, S., Miyatake, H., et al. 2023, *arXiv e-prints*, arXiv:2304.00703, doi: [10.48550/arXiv.2304.00703](https://doi.org/10.48550/arXiv.2304.00703)
- Murray, S. G., & Trott, C. M. 2018, *ApJ*, 869, 25, doi: [10.3847/1538-4357/aaebfa](https://doi.org/10.3847/1538-4357/aaebfa)
- Orosz, N., Dillon, J. S., Ewall-Wice, A., Parsons, A. R., & Thyagarajan, N. 2019, *MNRAS*, 487, 537, doi: [10.1093/mnras/stz1287](https://doi.org/10.1093/mnras/stz1287)
- Parsons, A., Pober, J., McQuinn, M., Jacobs, D., & Aguirre, J. 2012, *The Astrophysical Journal*, 753, 81, doi: [10.1088/0004-637X/753/1/81](https://doi.org/10.1088/0004-637X/753/1/81)
- Parsons, A. R., Pober, J. C., Aguirre, J. E., et al. 2012, *ApJ*, 756, 165, doi: [10.1088/0004-637X/756/2/165](https://doi.org/10.1088/0004-637X/756/2/165)
- Parsons, A. R., Backer, D. C., Foster, G. S., et al. 2010, *AJ*, 139, 1468, doi: [10.1088/0004-6256/139/4/1468](https://doi.org/10.1088/0004-6256/139/4/1468)
- Patil, A. H., Yatawatta, S., Koopmans, L. V. E., et al. 2017, *ApJ*, 838, 65, doi: [10.3847/1538-4357/aa63e7](https://doi.org/10.3847/1538-4357/aa63e7)
- Planck Collaboration, Adam, R., Ade, P. A. R., et al. 2016, *A&A*, 594, A1, doi: [10.1051/0004-6361/201527101](https://doi.org/10.1051/0004-6361/201527101)
- Planck Collaboration, Aghanim, N., Akrami, Y., et al. 2020, *A&A*, 641, A1, doi: [10.1051/0004-6361/201833880](https://doi.org/10.1051/0004-6361/201833880)
- Poer, J. C., Liu, A., Dillon, J. S., et al. 2014, *ApJ*, 782, 66, doi: [10.1088/0004-637X/782/2/66](https://doi.org/10.1088/0004-637X/782/2/66)
- Pritchard, J. R., & Loeb, A. 2012, *Reports on Progress in Physics*, 75, 086901, doi: [10.1088/0034-4885/75/8/086901](https://doi.org/10.1088/0034-4885/75/8/086901)
- Rahimi, M., Pindor, B., Line, J. L. B., et al. 2021, *MNRAS*, 508, 5954, doi: [10.1093/mnras/stab2918](https://doi.org/10.1093/mnras/stab2918)
- Rau, U., & Cornwell, T. J. 2011, *A&A*, 532, A71, doi: [10.1051/0004-6361/201117104](https://doi.org/10.1051/0004-6361/201117104)
- Riess, A. G., Filippenko, A. V., Challis, P., et al. 1998, *AJ*, 116, 1009, doi: [10.1086/300499](https://doi.org/10.1086/300499)
- Seljak, U. 1998, *ApJ*, 503, 492, doi: [10.1086/306019](https://doi.org/10.1086/306019)
- Sobacchi, E., & Mesinger, A. 2014, *MNRAS*, 440, 1662, doi: [10.1093/mnras/stu377](https://doi.org/10.1093/mnras/stu377)
- Staggs, S., Dunkley, J., & Page, L. 2018, *Reports on Progress in Physics*, 81, 044901, doi: [10.1088/1361-6633/aa94d5](https://doi.org/10.1088/1361-6633/aa94d5)
- Sullivan, I. S., Morales, M. F., Hazelton, B. J., et al. 2012, *ApJ*, 759, 17, doi: [10.1088/0004-637X/759/1/17](https://doi.org/10.1088/0004-637X/759/1/17)
- Tegmark, M. 1997, *PhRvD*, 55, 5895, doi: [10.1103/PhysRevD.55.5895](https://doi.org/10.1103/PhysRevD.55.5895)
- Tegmark, M., Hamilton, A. J. S., & Xu, Y. 2002, *MNRAS*, 335, 887, doi: [10.1046/j.1365-8711.2002.05622.x](https://doi.org/10.1046/j.1365-8711.2002.05622.x)
- Tingay, S. J., Goeke, R., Bowman, J. D., et al. 2013, *PASA*, 30, e007, doi: [10.1017/pasa.2012.007](https://doi.org/10.1017/pasa.2012.007)
- Trott, C. M., Pindor, B., Procopio, P., et al. 2016, *ApJ*, 818, 139, doi: [10.3847/0004-637X/818/2/139](https://doi.org/10.3847/0004-637X/818/2/139)

van Haarlem, M. P., Wise, M. W., Gunst, A. W., et al. 2013, *A&A*, 556, A2, doi: [10.1051/0004-6361/201220873](https://doi.org/10.1051/0004-6361/201220873)  
Virtanen, P., Gommers, R., Oliphant, T. E., et al. 2020, *Nature Methods*, 17, 261, doi: [10.1038/s41592-019-0686-2](https://doi.org/10.1038/s41592-019-0686-2)  
Wayth, R. B., Lenc, E., Bell, M. E., et al. 2015, *PASA*, 32, e025, doi: [10.1017/pasa.2015.26](https://doi.org/10.1017/pasa.2015.26)

Xu, Z., Hewitt, J. N., Chen, K.-F., et al. 2022, *ApJ*, 938, 128, doi: [10.3847/1538-4357/ac9053](https://doi.org/10.3847/1538-4357/ac9053)